Available online at www.sciencedirect.com
ScienceDirect
Journal of Computational Physics 224 (2007) 924–940
JOURNAL OF COMPUTATIONAL PHYSICS
www.elsevier.com/locate/jcp

Predicting the onset of flow unsteadiness based on global instability

J.D. Crouch [a,*], A. Garbaruk [b], D. Magidov [b]

[a] *Boeing Commercial Airplanes, P.O. Box 3707, MS 67-LF, Seattle 98124-2207, WA, USA*
[b] *Saint-Petersburg Polytechnic University, St.-Petersburg, Russia*

Received 5 July 2005; received in revised form 28 April 2006; accepted 30 October 2006
Available online 5 February 2007

Abstract

Global-stability theory is used to predict the onset of flow unsteadiness based on steady solutions of the Reynolds Averaged Navier–Stokes equations. The stability problem is formulated for compressible flow at moderately-high Reynolds numbers, using a turbulence model to provide closure for the averaged Reynolds stresses. The approach provides an efficient method for predicting the occurrence of flow unsteadiness for problems of practical interests, and provides a useful indicator for the legitimate range of application of the steady-flow equations. Numerical solutions are presented based on a finite-difference approximation. The steady baseflow solution and the unsteady disturbance equations are solved using the same grid. Results are presented for the onset of vortex shedding about a circular cylinder at low Reynolds numbers, and for shock-induced transonic-buffet onset at high Reynolds numbers. The results for the onset of flow unsteadiness are in very good agreement with experiments and unsteady calculations.

Keywords: Buffet; CFD; Global instability; Transonic flow; URANS; Unsteady flow; Vortex shedding

1. Introduction

Predicting the demarcation between steady- and unsteady-flow conditions is a fundamental problem that is critically important for many engineering flows, and for the efficient application of computational methods in general. The onset of large-scale flow unsteadiness is characterized by fluctuating loads that can be detrimental in engineering applications. Thus, engineering designs often require a prediction for the occurrence of these undesirable flow conditions. To alleviate or control the unsteadiness, a physical understanding of the underlying mechanisms is required.

In Computational Fluid Dynamics (CFD), steady-state equations are often used to investigate flow phenomena and to predict various integral quantities such as forces and moments. The solution of the steady-state

* Corresponding author. Tel.: +1 425 234 0975.
E-mail address: jeffrey.d.crouch@boeing.com (J.D. Crouch).

0021-9991/$ - see front matter © 2006 Published by Elsevier Inc.
doi:10.1016/j.jcp.2006.10.035

equations is much more efficient than solving the time-accurate problem, thus enabling the consideration of more-complex geometries. However, for some flow conditions the numerical representation of the steady-state equations may exhibit poor convergence. This can be the result of inherent unsteadiness in the flow. The ability to predict the onset of an underlying unsteadiness could be a valuable aid when applying CFD to such flows. At the very least, knowing the conditions for the onset of unsteadiness would enable an efficient switch over to the unsteady equations.

One of the most challenging problems involving the onset of large-scale unsteadiness is transonic-buffet onset on airplanes. At transonic speeds, a highly loaded wing will develop a strong compression shock – followed by boundary-layer separation upstream of the wing trailing edge. In some cases, a very thin separation bubble is created at the foot of the shock. At some point, as the loading is increased, the flow becomes highly unsteady – characterized by an oscillating shock position. This unsteady forcing can lead to significant buffeting of the airplane structure, thus limiting the airplane flight envelope.

Methods for predicting the onset of excess airplane buffeting (a structural response) are largely based on empirical relationships. However, studies on two-dimensional airfoils show many of the characteristic features associated with airplane buffeting. These airfoil studies serve as model problems for examining the onset of buffet, by focusing on the origins of large-scale flow unsteadiness. One of the earlier studies of this type was conducted by McDevitt and Okuno [1]. They examined the onset of unsteadiness on a NACA0012 airfoil undergoing a slow increase in angle of attack at constant Mach number. Meanwhile, this type of investigation was conducted on supercritical SC(2)-0714 [2] and OAT15A [3] airfoils. These studies demonstrate the existence of steady flow at lower angles of attack, giving way to large-scale buffeting above some critical value.

Unsteady CFD has been used to study the flow-field buffet onset, with some degree of success. Barakos and Drikakis [4] and Chung et al. [5] have analyzed the NACA0012 airfoil using the Unsteady Reynolds Averaged Navier–Stokes (URANS) equations. The critical angle of attack predicted by Chung et al. is in good agreement with the experiments of McDevitt and Okuno. The OAT15A airfoil has been investigated by Deck [6] using both URANS and Detached Eddy Simulations (DES). The computational results are in reasonable agreement with the experiments for post-critical conditions. However, the URANS required an increased angle of attack (compared to the experiments) in order to achieve buffeting flow conditions.

The application of URANS to find buffet boundaries requires the time-accurate integration of the RANS equations over a wide range of control parameters. For a moderately large design space (Reynolds number, Mach number, angle of attack, etc.) this exercise is very computationally intensive. In addition, obtaining an unsteady solution of the RANS equations is a subtle procedure that depends on the grid, the numerical method, and the way in which the flow is initialized. Near the critical conditions for buffet onset, unsteady disturbances amplify or decay over large time scales, further increasing the computational demands.

An attractive alternative to the URANS-based approach is to predict the onset of large-scale flow unsteadiness based on global-stability theory. As described above, this type of approach would be very useful for determining buffet boundaries in engineering. This capability would also be useful as an aid to the application of fully unsteady CFD, since it could provide a demarcation of the parameter space where unsteady calculations are required. The global-stability approach has been used to study a related problem of vortex-shedding onset for the incompressible laminar flow about a cylinder [7–9]. This approach has also been used to study a wide range of classic stability problems involving laminar basic states [10]. The application to transonic buffet [11] requires a generalization of that approach to incorporate turbulent boundary layers, compressibility, and the existence of shocks. This introduces a number of computational issues associated with the numerical solution of the background steady flow and the associated eigenvalue problem for the unsteady disturbance.

In this paper, we consider a generalized approach to predicting the onset of flow unsteadiness based on global-stability theory. The theoretical formulation is presented in Section 2. Section 3 describes the numerical method and the treatment of shocks. Results are presented in Section 4 for vortex shedding behind a circular cylinder and for transonic buffet on a NACA0012 airfoil. These two problems provide a wide range in level of complexity, from low-Reynolds-number laminar incompressible flow up to high-Reynolds-number turbulent compressible flow.

2. Theoretical formulation

2.1. Governing equations and turbulence modeling

We consider two-dimensional compressible flow, including relatively-high Reynolds numbers. The flow is governed by the Reynolds Averaged Navier–Stokes equations (RANS), with the compressible form of the Spalart–Allmaras (S–A) turbulence model [12] – including the compressibility correction [13] – used to provide closure for the averaged Reynolds stresses. Here, we focus on flows that can be treated as either laminar or "fully turbulent", which removes the need for the trip-term functions. This leads to a set of five equations: continuity, streamwise momentum, transverse momentum, energy, and a modified eddy-viscosity equation. These equations can be written in terms of the primitive variables, $q = \{\rho, u, v, T, \tilde{\nu}\}$ as follows:

$$\frac{\partial \rho}{\partial t} + \frac{\partial(\rho u)}{\partial x} + \frac{\partial(\rho v)}{\partial y} = 0, \tag{2.1.1}$$

$$\frac{\partial(\rho u)}{\partial t} + \frac{\partial(\rho u^2 + \rho RT)}{\partial x} + \frac{\partial(\rho uv)}{\partial y} = \frac{\partial}{\partial x}(\tau_{xx}) + \frac{\partial}{\partial y}(\tau_{xy}), \tag{2.1.2}$$

$$\frac{\partial(\rho v)}{\partial t} + \frac{\partial(\rho uv)}{\partial x} + \frac{\partial(\rho v^2 + \rho RT)}{\partial y} = \frac{\partial}{\partial x}(\tau_{xy}) + \frac{\partial}{\partial y}(\tau_{yy}), \tag{2.1.3}$$

$$\begin{aligned}\frac{\partial(\rho C_v T + 0.5\rho(u^2+v^2))}{\partial t} &+ \frac{\partial(\rho u C_p T + 0.5\rho u(u^2+v^2))}{\partial x} + \frac{\partial(\rho v C_p T + 0.5\rho v(u^2+v^2))}{\partial y} \\ &= \frac{\partial}{\partial x}\left(u\tau_{xx} + v\tau_{xy} + \lambda_{\text{eff}}\frac{\partial T}{\partial x}\right) + \frac{\partial}{\partial y}\left(u\tau_{xy} + v\tau_{yy} + \lambda_{\text{eff}}\frac{\partial T}{\partial y}\right),\end{aligned} \tag{2.1.4}$$

$$\begin{aligned}\frac{\partial \rho\tilde{\nu}}{\partial t} + \frac{\partial \rho u\tilde{\nu}}{\partial x} + \frac{\partial \rho v\tilde{\nu}}{\partial y} &= \rho C_{b1}(1-f_{t2})\tilde{S}\tilde{\nu} + \frac{1}{\sigma}\left[\nabla\cdot((\mu+\rho\tilde{\nu})\nabla\tilde{\nu}) + C_{b2}\rho(\nabla\tilde{\nu})^2\right] \\ &\quad - \rho\left(C_{w1}f_w - \frac{C_{b1}}{k^2}f_{t2}\right)\left(\frac{\tilde{\nu}}{d}\right)^2 - C_5\frac{\rho\tilde{\nu}^2 S^2}{\gamma RT}.\end{aligned} \tag{2.1.5}$$

Here ρ is the density, T is the temperature, and u, v are velocities in the x-, y-directions, respectively. R is the specific gas constant, C_v and C_p are the specific heat capacities of the gas at constant volume and pressure, respectively (both assumed to be constant), $\gamma = C_p/C_v$, and S is the magnitude of the strain tensor. The effective stress tensor is defined by the components

$$\tau_{xx} = 2\mu_{\text{eff}}\frac{\partial u}{\partial x} - \frac{2}{3}\mu_{\text{eff}}\left(\frac{\partial u}{\partial x} + \frac{\partial v}{\partial y}\right), \quad \tau_{xy} = \mu_{\text{eff}}\left(\frac{\partial u}{\partial y} + \frac{\partial v}{\partial x}\right), \quad \tau_{yy} = 2\mu_{\text{eff}}\frac{\partial v}{\partial y} - \frac{2}{3}\mu_{\text{eff}}\left(\frac{\partial u}{\partial x} + \frac{\partial v}{\partial y}\right) \tag{2.1.6}$$

and the effective dynamic viscosity μ_{eff} and effective heat conductivity λ_{eff}, are defined as

$$\mu_{\text{eff}} = \mu(T) + \rho\nu_{\text{t}}, \quad \lambda_{\text{eff}} = \frac{\mu(T)}{Pr} + \frac{\rho\nu_{\text{t}}}{Pr_{\text{t}}}. \tag{2.1.7}$$

Here $\mu = \mu(T)$ is the dynamic viscosity, Pr and Pr_{t} are the Prandtl number and the turbulent Prandtl number, respectively, and the eddy-viscosity ν_{t} is calculated using the S–A turbulence model [12], with the functions

$$
\begin{aligned}
&\nu_t = f_{v1}\tilde{\nu}, \quad f_{v1} = \frac{\chi^3}{\chi^3 + C_{v1}^3}, \quad \chi \equiv \frac{\tilde{\nu}}{\nu}, \quad \nu = \frac{\mu}{\rho},\\
&f_{t2} = C_{t3}\exp(-C_{t4}\chi^2),\\
&\tilde{S} = \Omega + f_{v2}\frac{\tilde{\nu}}{\kappa^2 d^2}, \quad f_{v2} = 1 - \frac{\chi}{1+\chi f_{v1}},\\
&f_w = g\left(\frac{1+C_{w3}^6}{g^6 + C_{w3}^6}\right)^{1/6.}, \quad g = r + C_{w2}(r^6 - r), \quad r = \frac{\tilde{\nu}}{\tilde{S}\kappa^2 d^2},
\end{aligned}
\tag{2.1.8}
$$

where Ω is the vorticity magnitude, and d is the distance to the wall. The standard constants for the model are as follows:

$$
\begin{aligned}
&\sigma = 2/3, \quad \kappa = 0.41, \quad C_{b1} = 0.1355, \quad C_{b2} = 0.622,\\
&C_{w1} = \frac{C_{b1}}{\kappa^2} + \frac{(1+C_{b2})}{\sigma}, \quad C_{w2} = 0.3, \quad C_{w3} = 2.0, \quad C_{v1} = 7.1,\\
&C_{t3} = 1.2, \quad C_{t4} = 0.5, \quad C_5 = 3.5.
\end{aligned}
\tag{2.1.9}
$$

The boundary conditions imposed on the surface of the body are

$$
\begin{aligned}
&u = v = 0,\\
&\frac{\partial\rho}{\partial n} = \frac{\partial T}{\partial n} = 0,\\
&\tilde{\nu} = 0,
\end{aligned}
\tag{2.1.10}
$$

where $\partial/\partial n$ is a derivative normal to the surface and the density condition is derived from the momentum equation. The far-field conditions used in the compressible computations involve not only the primary variables ρ, u, v, T, $\tilde{\nu}$ but also the Riemann invariants. These conditions, expressed in terms of the primary variables, are given as

$$
\begin{aligned}
&I_1 = V_n + \frac{2a}{(\gamma-1)} = k_x u + k_y v + \frac{2}{(\gamma-1)}\sqrt{\gamma RT},\\
&I_2 = V_n - \frac{2a}{(\gamma-1)} = k_x u + k_y v - \frac{2}{(\gamma-1)}\sqrt{\gamma RT},\\
&I_3 = V_\tau = k_y u - k_x v,\\
&I_4 = \frac{RT}{\rho^{\gamma-1}}.
\end{aligned}
\tag{2.1.11}
$$

Here k_x, k_y are the local directional cosines of the boundary normal. These conditions are imposed on the subsonic boundaries in the following way. On the inlet boundary, $\tilde{\nu}$ and invariants I_1, I_3, I_4 are given and I_2 is extrapolated from the computational domain. On the outlet boundary, $\tilde{\nu}$ and I_1, I_3, I_4 are extrapolated from the computational domain and I_2 is given.

2.2. Velocity decomposition

The state vector describing the total flow field can be decomposed into a steady state $\bar{q} = \{\bar{\rho}, \bar{u}, \bar{v}, \overline{T}, \bar{\tilde{\nu}}\}$ and an unsteady vector $q' = \{\rho', u', v', T', \tilde{\nu}'\}$, $q = \bar{q} + q'$. The vector $\bar{q}$ is a solution to the steady form of Eqs. (2.1.1)–(2.1.5) – that is with $\partial\bar{q}/\partial t \equiv 0$. The steady-state RANS equations are normally re-written in conservative form before solving them numerically.

For conditions close to steady state, the unsteady component q' can be considered a small perturbation to the vector $\bar{q}$. Substituting $q = \bar{q} + q'$ into Eqs. (2.1.1)–(2.1.5), canceling the terms governing $\bar{q}$, and linearizing the equations in terms of q' yields:

$$\frac{\partial \rho'}{\partial t}+\frac{\partial(\bar{\rho}u'+\rho'\bar{u})}{\partial x}+\frac{\partial(\bar{\rho}v'+\rho'\bar{v})}{\partial y}=0, \tag{2.2.1}$$

$$\frac{\partial(\bar{\rho}u'+\rho'\bar{u})}{\partial t}+\frac{\partial(\rho'\bar{u}^2+2\bar{\rho}\bar{u}u'+\bar{\rho}RT'+\rho'R\overline{T})}{\partial x}+\frac{\partial(\bar{\rho}\bar{u}v'+\bar{\rho}u'\bar{v}+\rho'\bar{u}\bar{v})}{\partial y}=\frac{\partial}{\partial x}(\tau'_{xx})+\frac{\partial}{\partial y}(\tau'_{xy}), \tag{2.2.2}$$

$$\frac{\partial(\bar{\rho}v'+\rho'\bar{v})}{\partial t}+\frac{\partial(\bar{\rho}\bar{u}v'+\bar{\rho}u'\bar{v}+\rho'\bar{u}\bar{v})}{\partial x}+\frac{\partial(\rho'\bar{v}^2+2\bar{\rho}\bar{v}v'+\bar{\rho}RT'+\rho'R\overline{T})}{\partial y}=\frac{\partial}{\partial x}(\tau'_{xy})+\frac{\partial}{\partial y}(\tau'_{yy}), \tag{2.2.3}$$

$$\begin{aligned}&\frac{\partial(\rho'(C_v\overline{T}+0.5(\bar{u}^2+\bar{v}^2))+\bar{\rho}(C_vT'+\bar{u}u'+\bar{v}v'))}{\partial t}+\frac{\partial((\bar{\rho}u'+\rho'\bar{u})(C_p\overline{T}+0.5(\bar{u}^2+\bar{v}^2))+\bar{\rho}\bar{u}(C_pT'+\bar{u}u'+\bar{v}v'))}{\partial x}\\&\quad+\frac{\partial((\bar{\rho}v'+\rho'\bar{v})(C_p\overline{T}+0.5(\bar{u}^2+\bar{v}^2))+\bar{\rho}\bar{v}(C_pT'+\bar{u}u'+\bar{v}v'))}{\partial y}\\&=\frac{\partial}{\partial x}(u'\bar{\tau}_{xx}+v'\bar{\tau}_{xy}+\bar{u}\tau'_{xx}+\bar{v}\tau'_{xy}+\phi'_x)+\frac{\partial}{\partial y}\left(u'\bar{\tau}_{xy}+v'\bar{\tau}_{yy}+\bar{u}\tau'_{xy}+\bar{v}\tau'_{yy}+\phi'_y\right),\end{aligned} \tag{2.2.4}$$

$$\begin{aligned}&\frac{\partial(\bar{\rho}\tilde{v}'+\rho'\bar{\tilde{v}})}{\partial t}+\frac{\partial(\bar{\rho}u'\bar{\tilde{v}}+\rho'\bar{u}\bar{\tilde{v}}+\bar{\rho}\bar{u}\tilde{v}')}{\partial x}+\frac{\partial(\bar{\rho}v'\bar{\tilde{v}}+\rho'\bar{v}\bar{\tilde{v}}+\bar{\rho}\bar{v}\tilde{v}')}{\partial y}\\&=\frac{\bar{\rho}\bar{\tilde{v}}}{\bar{\Omega}}\left[C_{b1}(1-\bar{f}_{t2})+C_{w1}\kappa^2\frac{\partial\bar{f}_w}{\partial r}\bar{r}^2\right]\left(\frac{\partial\bar{u}}{\partial y}-\frac{\partial\bar{v}}{\partial x}\right)\cdot\left(\frac{\partial u'}{\partial y}-\frac{\partial v'}{\partial x}\right)+\left[C_{b1}\left(1-\bar{f}_{t2}-\bar{\chi}\frac{\partial\bar{f}_{t2}}{\partial\chi}\right)\right.\\&\quad\left.+C_{b1}\bar{r}\left(\left(\bar{f}_{v2}+\bar{\chi}\frac{\partial\bar{f}_{v2}}{\partial\chi}\right)(1-\bar{f}_{t2})+2\bar{f}_{t2}+\bar{\chi}\frac{\partial\bar{f}_{t2}}{\partial\chi}\right)-C_{w1}\kappa^2\bar{r}\left(2\bar{f}_w+\bar{r}\frac{\partial\bar{f}_w}{\partial r}-\bar{r}^2\frac{\partial\bar{f}_w}{\partial r}\left(\bar{f}_{v2}+\bar{\chi}\frac{\partial\bar{f}_{v2}}{\partial\chi}\right)\right)\right]\bar{\rho}\bar{\tilde{S}}\tilde{v}'\\&\quad+\left[C_{b1}\left(1-\bar{f}_{t2}-\bar{\chi}\frac{\partial\bar{f}_{t2}}{\partial\chi}\right)+C_{b1}\bar{r}\left(\bar{\chi}\frac{\partial\bar{f}_{v2}}{\partial\chi}(1-\bar{f}_{t2})+\bar{f}_{t2}+\bar{\chi}\frac{\partial\bar{f}_{t2}}{\partial\chi}\right)-C_{w1}\kappa^2\bar{r}\left(\bar{f}_w-\frac{\partial\bar{f}_w}{\partial r}\bar{r}^2\bar{\chi}\frac{\partial\bar{f}_{v2}}{\partial\chi}\right)\right]\bar{\tilde{v}}\bar{\tilde{S}}\rho'\\&\quad+\frac{1}{\sigma}\left[\frac{\partial}{\partial x}\left((\mu+\bar{\rho}\bar{\tilde{v}})\frac{\partial\tilde{v}'}{\partial x}\right)+\frac{\partial}{\partial y}\left((\mu+\bar{\rho}\bar{\tilde{v}})\frac{\partial\tilde{v}'}{\partial y}\right)+\frac{\partial}{\partial x}\left(\frac{\partial\bar{\tilde{v}}}{\partial x}(\bar{\rho}\tilde{v}'+\rho'\bar{\tilde{v}})\right)+\frac{\partial}{\partial y}\left(\frac{\partial\bar{\tilde{v}}}{\partial y}(\bar{\rho}\tilde{v}'+\rho'\bar{\tilde{v}})\right)\right]\\&\quad+\frac{C_{b2}}{\sigma}\left[\left(\left(\frac{\partial\bar{\tilde{v}}}{\partial x}\right)^2+\left(\frac{\partial\bar{\tilde{v}}}{\partial y}\right)^2\right)\rho'+2\bar{\rho}\left(\frac{\partial\bar{\tilde{v}}}{\partial x}\frac{\partial\tilde{v}'}{\partial x}+\frac{\partial\bar{\tilde{v}}}{\partial y}\frac{\partial\tilde{v}'}{\partial y}\right)\right]-2C_5\frac{\bar{\rho}\bar{\tilde{v}}^2}{\gamma R\overline{T}}\left[\left(\frac{\partial\bar{u}}{\partial y}+\frac{\partial\bar{v}}{\partial x}\right)\cdot\left(\frac{\partial u'}{\partial y}+\frac{\partial v'}{\partial x}\right)\right.\\&\quad\left.+2\frac{\partial\bar{u}}{\partial x}\frac{\partial u'}{\partial x}+2\frac{\partial\bar{v}}{\partial x}\frac{\partial v'}{\partial x}\right]-2C_5\frac{\bar{\rho}\bar{\tilde{v}}\bar{\tilde{S}}^2}{\gamma R\overline{T}}\tilde{v}'-C_5\frac{\bar{\tilde{v}}^2\bar{\tilde{S}}^2}{\gamma R\overline{T}}\rho'+C_5\frac{\bar{\rho}\bar{\tilde{v}}^2\bar{\tilde{S}}^2}{\gamma R\overline{T}^2}T',\end{aligned} \tag{2.2.5}$$

where

$$\begin{aligned}\tau'_{xx}&=2\bar{\mu}_{\text{eff}}\left[\frac{\partial u'}{\partial x}-\frac{1}{3}\left(\frac{\partial u'}{\partial x}+\frac{\partial v'}{\partial y}\right)\right]+2\mu'_{\text{eff}}\left[\frac{\partial\bar{u}}{\partial x}-\frac{1}{3}\left(\frac{\partial\bar{u}}{\partial x}+\frac{\partial\bar{v}}{\partial y}\right)\right],\\\tau'_{xy}&=\bar{\mu}_{\text{eff}}\left(\frac{\partial u'}{\partial y}+\frac{\partial v'}{\partial x}\right)+\mu'_{\text{eff}}\left(\frac{\partial\bar{u}}{\partial y}+\frac{\partial\bar{v}}{\partial x}\right),\\\tau'_{yy}&=2\bar{\mu}_{\text{eff}}\left[\frac{\partial v'}{\partial y}-\frac{1}{3}\left(\frac{\partial u'}{\partial x}+\frac{\partial v'}{\partial y}\right)\right]+2\mu'_{\text{eff}}\left[\frac{\partial\bar{v}}{\partial y}-\frac{1}{3}\left(\frac{\partial\bar{u}}{\partial x}+\frac{\partial\bar{v}}{\partial y}\right)\right],\\\phi'_x&=\bar{\lambda}_{\text{eff}}\frac{\partial T'}{\partial x}+\lambda'_{\text{eff}}\frac{\partial\overline{T}}{\partial x},\quad\phi'_y=\bar{\lambda}_{\text{eff}}\frac{\partial T'}{\partial y}+\lambda'_{\text{eff}}\frac{\partial\overline{T}}{\partial y}\end{aligned} \tag{2.2.6}$$

and

$$\mu'_{\text{eff}}=\bar{\rho}\nu'_{\text{t}}+\rho'\bar{\nu}_{\text{t}}=\left(\bar{f}_{v1}+\bar{\chi}\frac{\partial\bar{f}_{v1}}{\partial\chi}\right)(\bar{\rho}\tilde{v}'+\rho'\bar{\tilde{v}}),\quad\lambda'_{\text{eff}}=\mu'_{\text{eff}}/Pr_{\text{t}}. \tag{2.2.7}$$

Eqs. (2.2.1)–(2.2.5) can be rewritten in the simplified operator form

$$\frac{\partial}{\partial t}M[q']+N_{\bar{q}}[q']=0. \tag{2.2.8}$$

The linear operator M contains the terms associated with the time derivatives from the original Eqs. (2.1.1)–(2.1.5). The linear operator $N_{\bar{q}}$ consists of linear terms from the original equations, and the terms generated by nonlinear interactions between $\bar{q}$ and q'.

2.3. Modal analysis

The unsteady perturbation to the steady-state flow $\bar{q}(x,y)$ can be represented by time-harmonic modes of the form

$$q'(x,y,t) = \hat{q}(x,y)\cdot\exp(-\mathrm{i}\omega t). \tag{2.3.1}$$

The function $\hat{q}$ describes the mode shape, and ω is the frequency. In general, both $\hat{q}$ and ω can be complex, so the physical solution is taken as the real part of Eq. (2.3.1). Substituting (2.3.1) into (2.2.8) yields a system governing the modal perturbation. Multiplying this system by the matrix W, where

$$W = \begin{pmatrix} 1 & 0 & 0 & 0 & 0 \\ -\frac{\bar{u}}{\bar{\rho}} & \frac{1}{\bar{\rho}} & 0 & 0 & 0 \\ -\frac{\bar{v}}{\bar{\rho}} & 0 & \frac{1}{\bar{\rho}} & 0 & 0 \\ -\frac{\overline{T}}{\bar{\rho}} + \frac{\bar{u}^2+\bar{v}^2}{2C_v\bar{\rho}} & -\frac{\bar{u}}{C_v\bar{\rho}} & -\frac{\bar{v}}{C_v\bar{\rho}} & \frac{1}{C_v\bar{\rho}} & 0 \\ -\frac{\bar{\tilde{v}}}{\bar{\rho}} & 0 & 0 & 0 & \frac{1}{\rho} \end{pmatrix} \tag{2.3.2}$$

yields the final system of equations for $\hat{q}$ and ω

$$-\mathrm{i}\omega\hat{q} + L(\bar{q})\cdot\hat{q} = 0 \tag{2.3.3}$$

with L being a second-order differential operator.

The boundary conditions are obtained by introducing $q = \bar{q} + q'$ into the expressions (2.1.10) and canceling the terms governing the steady state. Then substituting (2.3.1) for q' yields the boundary conditions for $\hat{q}$

$$\begin{aligned} &\hat{u} = \hat{v} = 0, \\ &\frac{\partial\hat{\rho}}{\partial n} = \frac{\partial\widehat{T}}{\partial n} = 0, \\ &\hat{\tilde{v}} = 0. \end{aligned} \tag{2.3.4}$$

The expressions for the Riemann invariants (2.1.11) become

$$\begin{aligned} \widehat{I}_1 &= k_x\hat{u} + k_y\hat{v} + \frac{\sqrt{\gamma R}}{(\gamma-1)\sqrt{\overline{T}}}\widehat{T}, \\ \widehat{I}_2 &= k_x\hat{u} + k_y\hat{v} - \frac{\sqrt{\gamma R}}{(\gamma-1)\sqrt{\overline{T}}}\widehat{T}, \\ \widehat{I}_3 &= k_y\hat{u} - k_x\hat{v}, \\ \widehat{I}_4 &= R\left(\frac{\widehat{T}}{\bar{\rho}^{\gamma-1}} - (\gamma-1)\frac{\overline{T}\hat{\rho}}{\bar{\rho}^{\gamma}}\right), \end{aligned} \tag{2.3.5}$$

which yields the following far-field conditions for the inlet boundary:

$$\begin{aligned} &\widehat{I}_1 = \widehat{I}_3 = \widehat{I}_4 = \hat{\tilde{v}} = 0, \\ &\frac{\partial\widehat{I}_2}{\partial n} = 0, \end{aligned} \tag{2.3.6}$$

and for the outlet boundary

$$\frac{\partial \widehat{I}_1}{\partial n} = \frac{\partial \widehat{I}_3}{\partial n} = \frac{\partial \widehat{I}_4}{\partial n} = \frac{\partial \hat{\tilde{\nu}}}{\partial n} = 0,$$
$$\widehat{I}_2 = 0. \tag{2.3.7}$$

Eqs. (2.3.3)–(2.3.7) describe an eigenvalue problem governing the complex frequency ω and mode shape $\hat{q}$. This eigenvalue problem is solved numerically.

3. Numerical formulation

3.1. Finite-difference approximation

We first introduce a finite-difference grid with the total number of nodes $N_p = N_i \times N_j$. The following one-dimensional ("global") numbering of the grid nodes is used:

$$n = N_j(i-1) + j \quad \text{with } n = 1, \ldots, N_p,$$
$$i = 1, \ldots, N_i, \quad j = 1, \ldots, N_j. \tag{3.1.1}$$

Now, let the vector $\hat{a}$ with the dimension $N_V = n_{\text{var}} \times N_p$ be the finite-difference analog of the perturbation mode shape ($n_{\text{var}} = 5$ is the number of the primary variables in the RANS equations)

$$\hat{a} = [\hat{q}_{11}, \hat{q}_{12}, \ldots, \hat{q}_{1N_j}, \ldots, \hat{q}_{N_iN_j}]^{\mathrm{T}}$$
$$\equiv [\hat{\rho}_{11}, \hat{u}_{11}, \hat{v}_{11}, \widehat{T}_{11}, \hat{\tilde{\nu}}_{11}, \ldots, \hat{\rho}_{1N_j}, \hat{u}_{1N_j}, \hat{v}_{1N_j}, \widehat{T}_{1N_j}, \hat{\tilde{\nu}}_{1N_j}, \ldots, \hat{\rho}_{N_iN_j}, \hat{u}_{N_iN_j}, \hat{v}_{N_iN_j}, \widehat{T}_{N_iN_j}, \hat{\tilde{\nu}}_{N_iN_j}]^{\mathrm{T}}, \tag{3.1.2}$$

or, using global node numbering (3.1.1)

$$\hat{a} = [\hat{\rho}_1, \hat{u}_1, \hat{v}_1, \widehat{T}_1, \hat{\tilde{\nu}}_1, \ldots, \hat{\rho}_n, \hat{u}_n, \hat{v}_n, \widehat{T}_n, \hat{\tilde{\nu}}_n, \ldots, \hat{\rho}_{N_p}, \hat{u}_{N_p}, \hat{v}_{N_p}, \widehat{T}_{N_p}, \hat{\tilde{\nu}}_{N_p}]^{\mathrm{T}}. \tag{3.1.3}$$

Then the finite-difference approximation of the system (2.3.3) and corresponding linearized boundary conditions (2.3.4) and (2.3.5) can be presented in the following matrix form:

$$(-\mathrm{i}\omega T + S) \cdot \hat{a} = 0, \tag{3.1.4}$$

where the matrix S with the dimension N_V is an approximation of the differential operator $L(\bar{q})$ on the computational grid.

The matrix T in (3.1.4) is diagonal ($T_{ml} = 0$ for $m \neq l$); its diagonal elements T_{mm} are equal to 0 for all m corresponding to the boundary points of the computational grid and for all other points $T_{mm} = 1$.

A similar formulation can be used for multi-block grids with global numbering extended to all blocks

$$n = \sum_{k=1}^{n_b - 1} N_p^{(k)} + N_j^{(n_b)}(i-1) + j, \tag{3.1.5}$$

with $N_p^{(n_b)} = N_i^{(n_b)} \times N_j^{(n_b)}$, $i = 1, \ldots, N_i^{(n_b)}$, $j = 1, \ldots, N_j^{(n_b)}$, $n_b = 1, \ldots, N_b$ – where N_b is the number of blocks.

Since the multi-block grids in the present work are overlapping, a specific boundary condition based on interpolation for points on grid-block interfaces is used. The form of this boundary condition is the same for both steady-flow and perturbation computations

$$\hat{a}_{i_b^{(n_{b1})}} = \sum_{i_b^{(n_{b2})}} \beta_{i_b^{(n_{b2})}} \hat{a}_{i_b^{(n_{b2})}}, \tag{3.1.6}$$

where $i_b^{(n_{b2})}$ are the indices of all points in the block n_{b2}, which correspond to the point $i_b^{(n_{b1})}$ in the block n_{b1} and $\beta_{i_b^{(n_{b2})}}$ are the interpolation coefficients.

The specific form of the matrix S depends upon the approximation of the space derivatives in the differential operator $L(\bar{q})$. In the present work, the steady RANS equations are solved using Roe's scheme [14] with the third-order κ scheme [15] for inviscid fluxes and a second-order central difference scheme for viscous and heat fluxes. Convection terms in the S–A equation are approximated with the first-order upwind scheme. The

only modification of the scheme used for the solution of the system (2.3.3) is that, unlike the original Roe scheme, the upwind finite-difference approximations are linearized and are based on the sign of the cell-face normal component of the steady velocity.

Convective terms in the system (2.3.3) can be written in the following form:

$$\left(\frac{\partial F}{\partial x}\right)+\left(\frac{\partial G}{\partial y}\right)=\frac{\partial}{\partial x}(A(\bar{q})\cdot\hat{q})+\frac{\partial}{\partial y}(B(\bar{q})\cdot\hat{q}). \tag{3.1.7}$$

In curvilinear coordinates this becomes

$$\frac{\partial F}{\partial x}+\frac{\partial G}{\partial y}=J\left(\frac{\partial \widetilde{F}}{\partial s}+\frac{\partial \widetilde{G}}{\partial n}\right), \tag{3.1.8}$$

where J is the Jacobian

$$J=\frac{\partial s}{\partial x}\cdot\frac{\partial n}{\partial y}-\frac{\partial s}{\partial y}\cdot\frac{\partial n}{\partial x}. \tag{3.1.9}$$

Generalized fluxes $\widetilde{F},\ \widetilde{G}$ are defined as

$$\begin{aligned}\widetilde{F}&=X_nF+Y_nG=(X_nA(\bar{q})+Y_nB(\bar{q}))\cdot\hat{q}=\widetilde{A}(\bar{q})\cdot\hat{q},\\ \widetilde{G}&=X_sF+Y_sG=(X_sA(\bar{q})+Y_sB(\bar{q}))\cdot\hat{q}=\widetilde{B}(\bar{q})\cdot\hat{q},\end{aligned} \tag{3.1.10}$$

where $X_n,\ Y_n,\ X_s,\ Y_s$ are the metric coefficients

$$X_n=\frac{\partial y}{\partial n},\quad Y_n=-\frac{\partial x}{\partial n},\quad X_s=-\frac{\partial y}{\partial s},\quad Y_s=\frac{\partial x}{\partial s}. \tag{3.1.11}$$

The finite-difference formulation of Eq. (3.1.8) then has the form

$$\begin{aligned}\frac{\partial \widetilde{F}}{\partial s}+\frac{\partial \widetilde{G}}{\partial n}&=\widetilde{F}_{i+1/2,j}-\widetilde{F}_{i-1/2,j}+\widetilde{G}_{i,j+1/2}-\widetilde{G}_{i,j-1/2}\\ &=\widetilde{A}(\bar{q})_{i+1/2,j}\cdot\hat{q}_{i+1/2,j}-\widetilde{A}(\bar{q})_{i-1/2,j}\cdot\hat{q}_{i-1/2,j}+\widetilde{B}(\bar{q})_{i,j+1/2}\cdot\hat{q}_{i,j+1/2}-\widetilde{B}(\bar{q})_{i,j-1/2}\cdot\hat{q}_{i,j-1/2}.\end{aligned} \tag{3.1.12}$$

The central-difference scheme is based on the following expression for the cell face flux:

$$\widetilde{A}(\bar{q})_{i+1/2,j}\cdot\hat{q}_{i+1/2,j}=\frac{1}{2}\left(\widetilde{A}^{+}_{i+1/2,j}\cdot\hat{q}^{+}_{i+1/2,j}+\widetilde{A}^{-}_{i+1/2,j}\cdot\hat{q}^{-}_{i+1/2,j}\right). \tag{3.1.13}$$

The cell-face flux for upwind scheme has the form

$$\widetilde{A}(\bar{q})_{i+1/2,j}\cdot\hat{q}_{i+1/2,j}=\frac{1}{2}\left(\left(1-\operatorname{sign}\left((\bar{u}_s)_{i+1/2,j}\right)\right)\widetilde{A}^{+}_{i+1/2,j}\cdot\hat{q}^{+}_{i+1/2,j}+\left(1-\operatorname{sign}\left((\bar{u}_s)_{i+1/2,j}\right)\right)\widetilde{A}^{-}_{i+1/2,j}\cdot\hat{q}^{-}_{i+1/2,j}\right), \tag{3.1.14}$$

where $\bar{u}_s$ is the cell-face normal velocity component for the steady-state solution

$$\bar{u}_s=X_n\bar{u}+Y_n\bar{v}. \tag{3.1.15}$$

The order of approximation is dependent on the interpolation of vector $\hat{q}$ and matrix $\widetilde{A}$ on the cell-face $(i+1/2,j)$. The third-order upwind and fourth-order centered schemes used in the present work are based on the following expressions:

$$\hat{q}^{-}_{i+1/2,j}=\sum_{l=i-1}^{i+1}\alpha^{-}_l\hat{q}_{l,j},\quad \hat{q}^{+}_{i+1/2,j}=\sum_{l=i}^{i+2}\alpha^{+}_l\hat{q}_{l,j}, \tag{3.1.16}$$

$$\widetilde{A}^{-}_{i+1/2,j}=\sum_{l=i-1}^{i+1}\alpha^{-}_l\widetilde{A}_{l,j},\quad \widetilde{A}^{+}_{i+1/2,j}=\sum_{l=i}^{i+2}\alpha^{+}_l\widetilde{A}_{l,j}, \tag{3.1.17}$$

where

$$\begin{aligned} \alpha_{i-1}^{-} &= \alpha_{i+2}^{+} = -1/6, \\ \alpha_{i}^{-} &= \alpha_{i+1}^{+} = 5/6, \\ \alpha_{i+1}^{-} &= \alpha_{i}^{+} = 1/3. \end{aligned} \tag{3.1.18}$$

In order to reduce the numerical dissipation of the upwind differencing, we use a "hybrid" scheme which is weighted between upwind and central differencing

$$\Delta_{\mathrm{H}} = \alpha_{\mathrm{H}}\Delta_{3u} + (1-\alpha_{\mathrm{H}})\Delta_{4c}, \quad 0 \leqslant \alpha_{\mathrm{H}} \leqslant 1. \tag{3.1.19}$$

The finite difference operators Δ_{3u} and Δ_{4c} correspond to the third-order upwind and fourth-order centered schemes respectively and α_{H} is the weighting constant. Results are presented for $\alpha_{\mathrm{H}} = 0$, 1, and 0.2.

3.2. Treatment of shocks

In order to consider transonic flows with shock waves, some form of shock smoothing is required. An unsteady perturbation to a flow field containing a shock can be expected to have a large response at the shock location. As a shock is better resolved it will become thinner, and the unsteady response to a perturbation will take the form of a delta function. A typical steady-flow solution captures the shock over two or three grid points. Without smoothing, a linear perturbation to this flow field will exhibit "ringing" in the neighborhood of the shock.

We perform shock smoothing after the steady flow is calculated. The smoothing is conducted in two steps. First, the original solution to the steady RANS equations is smoothed over the entire computational domain, resulting in a smoothed field $\bar{q}_{\mathrm{smooth}}$. In the second step, the smoothed field is blended with the original field $\bar{q}_{\mathrm{original}}$ according to the relationship

$$\bar{q}_{\mathrm{final}} = (1-S)\bar{q}_{\mathrm{original}} + S\bar{q}_{\mathrm{smooth}}. \tag{3.2.1}$$

The blending function S takes a value of one at the shock, and smoothly transitions to zero away from the shock. The width of the smoothing zone is confined to a narrow region around the shock, where the grid spacing is very fine.

The flow-field smoothing during the first step is performed in the dominant flow direction, along grid lines. The smoothing is done over N_{SC} smoothing cycles. During each cycle, the flow variables are modified according to

$$\bar{q}(i,j) = \bar{q}(i,j) + 0.5c_i[\bar{q}(i+1,j) - 2\bar{q}(i,j) + \bar{q}(i-1,j)], \tag{3.2.2}$$

where c_i is a smoothing coefficient that controls the amount of smoothing per cycle. The field $\bar{q}_{\mathrm{smooth}}$ in (3.2.1) is defined by the value of $\bar{q}$ from (3.2.2) after N_{SC} smoothing cycles. For all of the results presented in this paper, $c_i = 0.1$. The effects of grid smoothing and the local grid spacing at the shock are considered in Section 4.2.

3.3. Eigenvalue calculations

The eigenvalue problem (3.1.4) is solved using the implicitly restarted Arnoldi method [16], which is a member of the Krylov subspace projection methods. After discretization, the matrix governing the eigenvalues is large and sparse, with typical dimension $\mathrm{O}(100,000)$. The Krylov methods are very efficient for calculating a small set of eigenvalues for such large systems, while requiring minimal storage. Prior to solution, a spectral transformation is used to transform the eigenvalues in the neighborhood of ω^* into extreme values for the system. This is achieved using the ARPACK routines [16] with the shift-invert mode.

Instability, signifying the onset of unsteadiness, occurs when $\omega_i > 0$. The eigenvalue calculations are focused on the least-stable mode. The value of the prescribed frequency ω_r^* is chosen based on experimental data, where available, or based on the basic model scaling for a given type of unsteadiness. The prescribed growth rate ω_i^* is taken to be positive. By varying the prescribed frequency, a search can be made for all unstable modes over a given range.

4. Results

The stability problem formulated in Sections 2 and 3 provides a general framework for predicting the onset of flow unsteadiness for compressible flow including high Reynolds number flows. This approach is now assessed by considering two example problems, which serve as limiting cases in terms of their level of complexity. First, we consider vortex shedding for a circular cylinder. This is a low-Reynolds-number laminar-flow condition at an essentially-incompressible Mach number. The second problem considered is transonic buffet onset for a NACA0012 airfoil. This is a high-Reynolds-number turbulent-flow condition, which includes shock waves.

The presented results are normalized using the following scales. The reference temperature T_0 is equal to the temperature in the incident flow, the reference length L_0 is equal to 1 m, and the reference scales for velocity, dynamic viscosity and density are defined as

$$V_0 = M\sqrt{\gamma R T_0},$$
$$\mu_0 = \mu(T_0),$$
$$\rho_0 = Re\frac{\mu_0}{L_0 V_0},$$

where M is the Mach number and Re is the Reynolds number.

4.1. Vortex shedding

Vortex shedding from a circular cylinder at low Reynolds numbers was one of the first problems considered using concepts of global-instability analysis [7–9]. We revisit this problem as a simple test case for the current formulation, and to provide updated estimates for the onset of instability. At low Reynolds numbers the flow is laminar, so the state vector reduces to $q = \{\rho, u, v, T\}$. The Mach number is also small, and is taken to be $M = 0.2$.

A typical grid used for the circular-cylinder calculations has 240 points in both the radial and azmuthal directions. The domain extends to 125 diameters. Contours of u-velocity for the steady flow around the cylinder are shown in Fig. 1, for the Reynolds number $Re = UD/\nu = 45$. This flow is stable to small unsteady perturbations. However, as the Reynolds number is increased the flow goes unstable – signifying the onset of vortex shedding.

The eigenvalue problem (3.1.4) yields a large number of eigenvalues, but only a small number of these are physically meaningful. We focus on the least-stable eigenmode as an indicator for the onset of unsteadiness. A small number of modes are calculated in the neighborhood of ω^*, where $\omega_i^* > 0$. Physical modes are distinguished from spurious modes by calculating the average eigenfunction amplitude at the far-field bound-

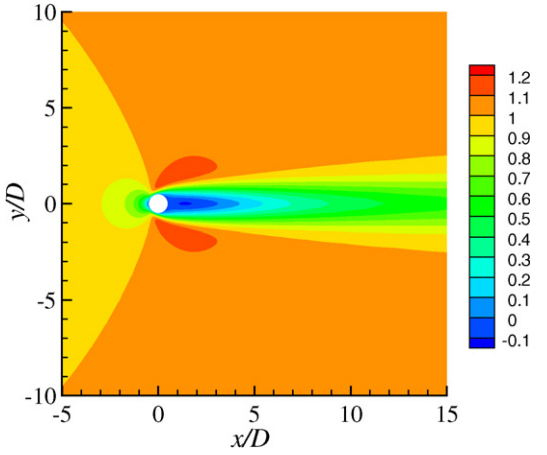

Fig. 1. Contours of the u-component of the mean velocity for the conditions: $Re = 45$, $M = 0.2$.

ary (neglecting the wake region). The physical modes have a negligibly small amplitude in the far field compared to the peak modal amplitude.

For this low-Mach-number flow, the instabilities can be calculated using the pure central-difference scheme ($\alpha_H = 0$), as well as the hybrid scheme ($\alpha_H = 0.2$) or the upwind scheme ($\alpha_H = 1$). Table 1 shows the most unstable eigenvalue calculated with the different schemes for the conditions $M = 0.2$, $Re = 60$. Results are given for several different grids, ranging from 6400 points up to 160,000 points. The results for the different numerical schemes converge to the same result on the finest grid to within 4 significant digits. Results for a significantly larger domain, extending to 200 diameters, differ by less than 0.5% for the most-unstable eigenvalue with a grid comparable to 240×240. All subsequent results are for the 125 diameter domain.

The mode shape for the least-stable eigenvalue is given in Fig. 2, for the 240×240 grid with $Re = 60$. The figure shows contours of the real part of the u-velocity component real($\hat{u}$). The imaginary part of $\hat{u}$ has the same form as the real part, except the maximum and minimum values occur at the location of the zeros in real($\hat{u}$). When the eigenfunction (with a large prescribed amplitude) is combined with the mean flow, the total unsteady flow field shows the typical vortex-shedding pattern.

The Reynolds-number variation of the least-stable eigenmode is given in Fig. 3. Unsteadiness due to vortex shedding is predicted to occur at $Re = 47$, where ω_i crosses zero. This is in very good agreement with the experimental results of Hammache and Gharib [17], which shows a critical value of $Re \approx 47$. This is also in good agreement with the numerical simulations of Barkley and Henderson [18], which give a critical Reynolds number of $Re \approx 46 \pm 1$. The original global-stability results of Jackson [7] showed a critical Reynolds number of $Re = 45.4$.

The frequency of unsteadiness is shown in Fig. 3(b), along with the experimental values taken from Williamson [19] and Hammache and Gharib [17]. The critical frequency is $\omega_r = 0.728$, which corresponds to a Strouhal number of $S = \omega_r/2\pi = 0.116$. The predictions are in very good agreement with the experiments near

Table 1
Eigenvalues for the circular cylinder with different grids at $M = 0.2$, $Re = 60$

Grid	$\alpha_H = 0$	$\alpha_H = 0.2$	$\alpha_H = 1$
80×80	0.7614, 0.0342	0.7603, 0.0331	0.7564, 0.0277
160×160	0.7434, 0.0425	0.7432, 0.0424	0.7425, 0.0418
240×240	0.7399, 0.0435	0.7398, 0.0435	0.7396, 0.0433
320×320	0.7388, 0.0438	0.7387, 0.0438	0.7386, 0.0437
400×400	0.7383, 0.0439	0.7383, 0.0439	0.7382, 0.0439

Comparison between the central-difference ($\alpha_H = 0$), hybrid ($\alpha_H = 0.2$), and upwind ($\alpha_H = 1$) schemes.

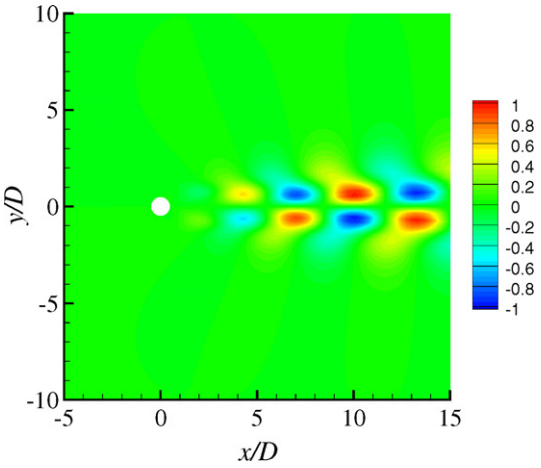

Fig. 2. Contours of the real part of the u-velocity perturbation for the conditions: $Re = 60$, $M = 0.2$ ($\alpha_H = 0$).

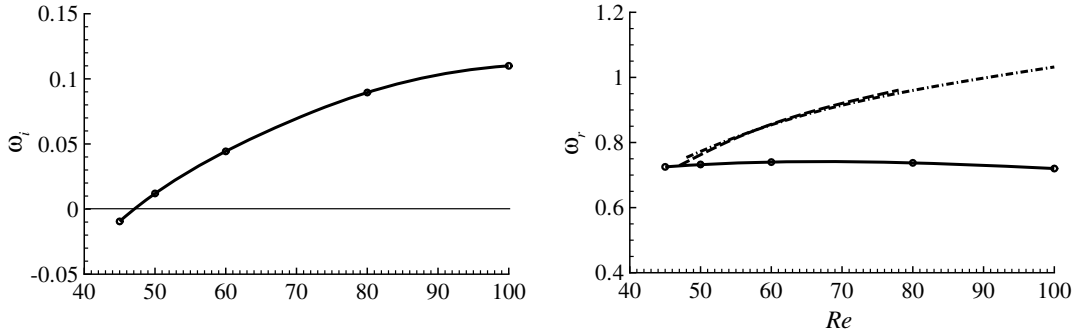

Fig. 3. Variation of the least-stable eigenvalue with Reynolds number for the conditions: $M = 0.2$ ($\alpha_H = 0$). Also shown are experimental values for the frequency taken from [17] – dashed line, and [19] – dash-dot line.

the onset of unsteadiness. The original results of Jackson [7] gave a critical Strouhal frequency of $S = 0.136$. As the Reynolds number is increased beyond the critical value, the experiments show a rise in the frequency that is not predicted by the theory. This is likely due to finite-amplitude effects that are neglected in the linear theory.

Unsteady calculations are made using the NTS code [20], which is the code used for generating the steady-state fields $\bar{q}$. The unsteady flow is started from a steady solution at $Re = 50$. The temporal variation of the v-velocity, measured at $x/D = 2$, $y/D = 0$, yields a frequency of 0.734 and a growth rate of 0.0096. The global-stability theory predicts a frequency $\omega_r = 0.735$ and a growth rate of $\omega_i = 0.0096$ at $Re = 50$; this is in good agreement with the unsteady calculations, and the small differences are attributed to differences in numerical discretization. A similar unsteady calculation at $Re = 70$ yields a frequency of 0.739 and a growth rate of 0.068. This compares well with the stability results, where $\omega_r = 0.745$ and $\omega_i = 0.068$. After the initial growth of the unsteady fluctuations, the unsteady calculations yield a shedding frequency of 0.901 – in very good agreement with the experiments (see Fig. 3). Overall, the global-stability theory is quite effective at predicting the onset and initial characteristics of vortex shedding.

4.2. Transonic buffet

To examine the potential for predicting transonic-buffet onset using the global-stability theory, we consider the NACA0012 airfoil. This problem was considered earlier in the experiments of McDevitt and Okuno [1] and in the unsteady calculations of Barakos and Drikakis [4] and Chung et al. [5]. The transonic flow around a NACA0012 airfoil at an angle of attack $\alpha > 2^\circ$ exhibits a shockwave on the upper surface. As the angle of attack is increased, the shock intensifies and the flow separates from the airfoil upper surface upstream of the trailing edge. A further increase in the angle of attack results in the forward movement of the separation point from the trailing edge toward the foot of the shock. When the angle of attack exceeds some critical value, the flow becomes globally unsteady. The unsteadiness is characterized by a coupled modulation of the shockwave and the separated shear layer.

The transonic-airfoil calculations are done at relatively high chord Reynolds numbers $Re = Uc/\nu$, where the boundary layers would typically be turbulent. For these flows the state vector is given by $q = \{\rho, u, v, T, \tilde{\nu}\}$. To capture the shock position (including small changes due to changes in α) a fine grid is required on the upper surface of the airfoil. In this study, we refine the grid in the neighborhood of the of the shock with a chordwise spacing of Δx_s. A typical grid is shown in Fig. 4, where $\Delta x_s/c = 0.0015$.

Fig. 5 shows the Mach contours for the flow around the NACA0012 airfoil at $Re = 10^7$, $M = 0.76$, and $\alpha = 3.2$ calculated using the grid of Fig. 4. At these conditions there is a strong shock at $x/c \approx 0.45$. To calculate the stability of this flow, we smooth the shock as discussed in Section 3.2. Fig. 6 shows contours of pressure in the neighborhood of the shock before smoothing, and after smoothing with $N_{SC} = 160$. The shock occurs over 2 grid points prior to smoothing, but extends over 10 points after smoothing. After smoothing, the variation of flow quantities across the shock is similar to experimental observations [21], except that the shock thickness is several orders of magnitude too large.

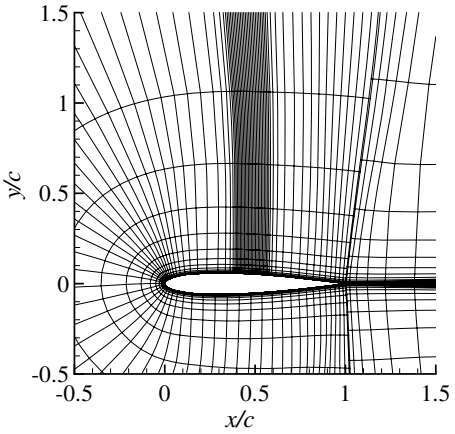

Fig. 4. Typical grid used for NACA0012 calculations (showing every 5th point).

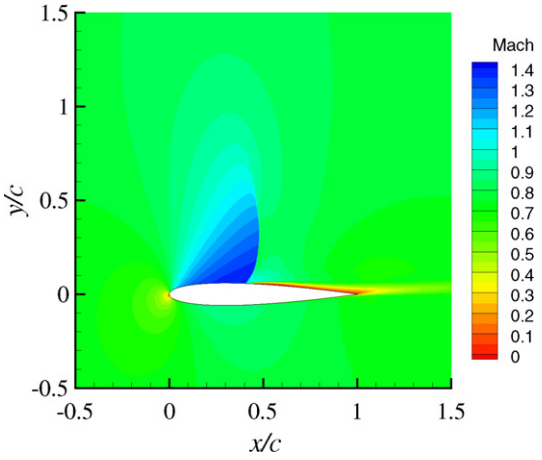

Fig. 5. Mach number contours for the steady flow around the NACA0012 airfoil at the conditions: $Re = 10^7$, $M = 0.76$, $\alpha = 3.2^\circ$.

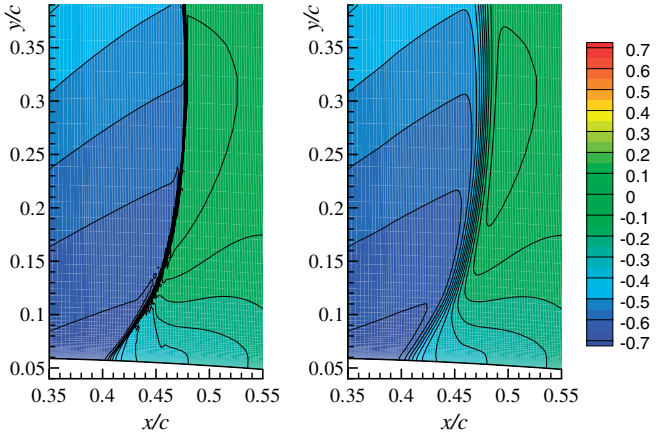

Fig. 6. Pressure contours showing the effect of shock smoothing, with: $N_{SC} = 0$, $N_{SC} = 160$ ($Re = 10^7$, $M = 0.76$, $\alpha = 3.2^\circ$).

For $Re = 10^7$, $M = 0.76$ the flow at $\alpha = 3.0$ is stable to temporal perturbations. However, as the angle of attack is increased the flow becomes less stable – as shown in Fig. 7. This figure shows the eigenvalues in the neighborhood of $\omega^* = (0.30, 0.15)$ for three different angles of attack. For lower angles of attack, all the modes are stable. At $\alpha \approx 3.03$ the least stable eigenvalue crosses the real axis, signifying the onset of instability due to a Hopf bifurcation. A further increase in the angle of attack results in an increase in the instability growth rate. The initial frequency of oscillation is $\omega_r = 0.28$. Calculations conducted with the same mean flow, but without including the $\tilde{\nu}$ perturbation equation, do not show any unstable modes near this angle of attack.

These results are based on $N_{SC} = 160$ and $\alpha_H = 0.2$. The value of the hybrid-scheme weighting constant α_H is chosen based on inspection of the eigenmodes. If the numerical dissipation if too small (i.e. $\alpha_H < 0.1$), the eigenmodes exhibit oscillations emanating from the shock. The eigenvalue dependence on α_H is small compared to other influences, such as the treatment of the shock. The effect of shock smoothing is discussed below.

The instability mode shape at $Re = 10^7$, $M = 0.76$, $\alpha = 3.2$ is shown in Fig. 8. The perturbation is concentrated around the shock and in the boundary layer downstream of the shock. The disturbance maximum at the shock is roughly two orders of magnitude larger than in the rest of the flow. Qualitatively, the instability represents an oscillation of the shock position. The phase plot shows that as the shock moves downstream, the

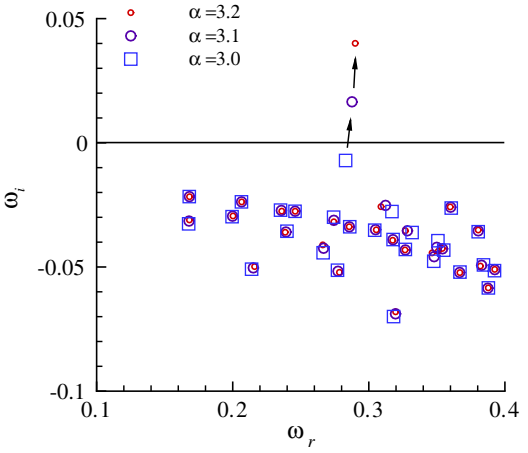

Fig. 7. Eigenvalues for $Re = 10^7$, $M = 0.76$ with different angles of attack $\alpha = 3.0°, 3.1°, 3.2°$. Onset of instability occurs at $\alpha \approx 3.03$.

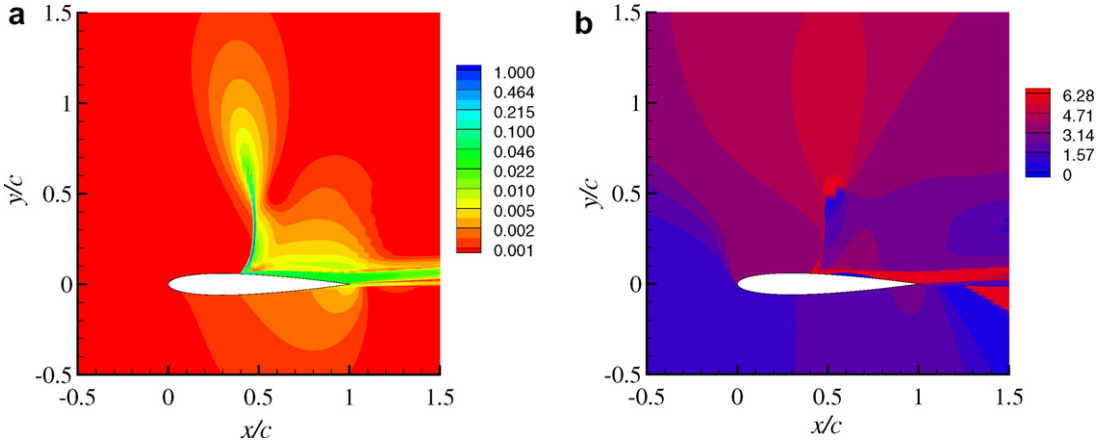

Fig. 8. u-velocity magnitude and phase for the unsteady-mode eigenfunction. NACA0012 airfoil results at the conditions: $Re = 10^7$, $M = 0.76$, $\alpha = 3.2°$ ($\alpha_H = 0.2$).

separated shear layer moves closer to the surface of the airfoil. When the shock moves forward, the shear layer lifts off of the surface. This form of oscillation is in good agreement with the observations of McDevitt and Okuno [1].

The stability results of Figs. 7 and 8 are based on the steady flow on a grid with $\Delta x_s/c = 0.0015$ and $N_{SC} = 160$. The eigenvalue results are found to be sensitive to both the grid spacing at the shock, and the number of smoothing cycles. However, the eigenvalue results for different grid spacing and different levels of shock smoothing collapse when plotted against the shock thickness $\epsilon_P = \max_{x,y}(\Delta P)/\max_{x,y}(\partial P/\partial x)$; here ΔP is the pressure jump across the shock and ϵ_P is nondimensionalized by the chord c. Eigenvalue results are shown in Fig. 9, for four different grids with four different levels of smoothing: $N_{SC} = 80$, 160, 240, 320. Larger grid spacing, or increased smoothing cycles, both lead to a thicker shock. The frequency is reduced with reduced shock thickness, until a minimum is reached and then increases with reduced shock thickness. The growth-rate variation is relatively flat for small shock thicknesses, but then shows a decrease with increasing shock thickness.

The results at different angles of attack all vary in a similar way, such that the critical α for onset of unsteadiness is not very sensitive to the shock thickness. Thus, the prediction of stability boundaries does not depend strongly on the grid or the level of smoothing. However, the critical frequency does show some dependence on these quantities. Comparing results with $N_{SC} = 80$ to results with no shock smoothing, the critical α changes by less than 0.03° and the critical frequency varies by roughly 4%. This variation in frequency is considered

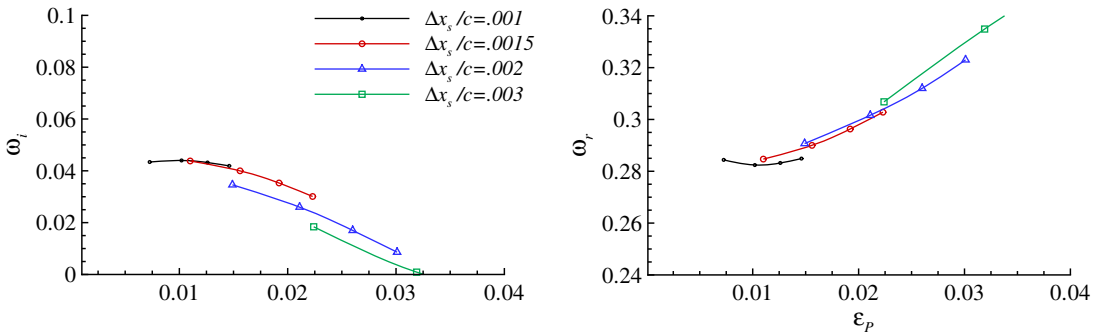

Fig. 9. Variation of the least-stable eigenvalue with the shock thickness for different grids and different numbers of smoothing cycles ($N_{SC} = 80$, 160, 240, 320; shown by symbols). NACA0012 airfoil results at the conditions: $Re = 10^7$, $M = 0.76$, $\alpha = 3.2°$ ($\alpha_H = 0.2$).

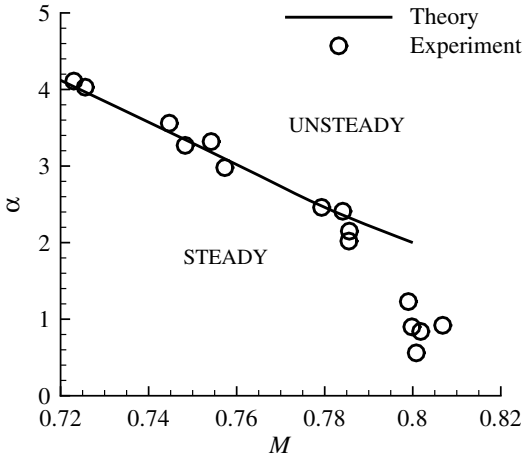

Fig. 10. Buffet boundary (α, M) for the NACA0012 airfoil at $Re = 10^7$ ($\alpha_H = 0.2$). Experimental results from [1].

insignificant compared to the potential nonlinear effects that can result from a moderate displacement of the shock due to unsteadiness.

Fig. 10 shows the predicted buffet boundary for the NACA0012 airfoil at a Reynolds number of $Re = 10^7$. For a given Mach number, there is a critical angle of attack – above which the flow becomes unsteady. The symbols show the experimental results of McDevitt and Okuno [1]. For most Mach numbers, the agreement with the experiment is very good. At the highest Mach number the experiment shows a lower value for the critical angle of attack. This motivated a search for other modes of instability, but no modes with a lower α_{crit} were found. The differences at the highest Mach numbers could be the result of an inadequate prediction of the steady flow due, for example, to turbulence modeling. However, these differences could also be due to experimental uncertainties. None-the-less, the overall agreement between the theory and experiment in Fig. 10 shows the stability theory to be an effective means for predicting the onset of transonic airfoil buffet.

5. Conclusions

Global-stability theory provides an effective and efficient means for predicting the onset of flow unsteadiness. The initial unsteadiness results from the instability of an underlying steady-state flow condition. For low Reynolds numbers, the underlying steady flow is laminar and the steady-state flow field is obtained by solving the full Navier–Stokes equations. At higher Reynolds numbers, the boundary layers and separated shear layers can be turbulent. In this case, the RANS equations must be solved to determine the underlying steady-state field.

The approach has been applied to two problems of practical interest: vortex shedding and transonic-buffet onset. The vortex shedding occurs at a low Reynolds number, and has been analyzed using global-stability analysis in earlier studies. Transonic buffet occurs at higher Reynolds numbers and requires the use of a turbulence model. For transonic flows with shocks, shock smoothing is used to ensure a smooth modal response. However, the conditions at which buffet onset occurs are found to be insensitive to the level of smoothing. Thus, no smoothing is required for a simple identification of the buffet boundary. Results from the stability theory are in good agreement with unsteady calculations and with experiments for both problems considered.

Acknowledgments

We are grateful to Steve Allmaras for reviewing a draft of this paper.

References

[1] J.B. McDevitt, A.F. Okuno, Static and dynamic pressure measurements on a NACA0012 airfoil in the Ames high Reynolds number facility, NASA Tech. Paper No. 2485, 1985.
[2] R.E. Bartels, J.W. Edwards, Cryogenic tunnel pressure measurements on a supercritical airfoil for several shock buffet conditions, NASA Tech. Mem. 110272, 1997.
[3] L. Jacquin, P. Molton, S. Deck, B. Maury, D. Soulevant, An experimental study of shock oscillation over a transonic supercritical profile, AIAA Paper No. 2005-4902, 2005.
[4] G. Barakos, D. Drikakis, Numerical simulation of transonic buffet flows using various turbulence closures, Int. J. Heat Fluid Flow 21 (2000) 620–626.
[5] I. Chung, D. Lee, T. Reu, Prediction of transonic buffet onset for an airfoil with shock induced separation bubble using steady Navier–Stokes solver, AIAA Paper No. 2002-2934, 2002.
[6] S. Deck, Detached-eddy simulation of transonic buffet over a supercritical airfoil, AIAA Paper No. 2004-5378, 2004.
[7] C.P. Jackson, A finite-element study of the onset of vortex shedding in flow past variously shaped bodies, J. Fluid Mech. 182 (1987) 23–45.
[8] A. Zebib, Stability of viscous flow past a circular cylinder, J. Eng. Math. 21 (1987) 55–165.
[9] D.C. Hill, A theoretical approach for analyzing the restabilization of wakes, AIAA Paper No. 92-0067, 1992.
[10] V. Theofilis, Advances in global linear instability analysis of nonparallel and three-dimensional flows, Prog. Aerospace Sci. 39 (2003) 249–315.
[11] J.D. Crouch, A. Garbaruk, M. Shur, M. Strelets, Predicting buffet onset from the temporal instability of steady RANS solutions, Bull. Am. Phys. Soc. 47 (2002) 68.
[12] P.R. Spalart, S.R. Allmaras, A one-equation turbulence model for aerodynamic flows, La Recherche Aérospatiale 1 (1994) 5–21 (also AIAA Paper No. 92-0439).

[13] P.R. Spalart, Trends in turbulence treatments, AIAA Paper No. 2000-2306, 2000.
[14] P.L. Roe, Approximate Riemann solvers, parameters vectors and difference schemes, J. Comput. Phys. 43 (1981) 357–372.
[15] B. van Leer, Upwind-difference methods for aerodynamic problems governed by the Euler equations, in: B. Enquist, S. Osher, R. Somerville (Eds.), Large Scale Computations in Fluid Mechanics, Lectures in Applied Mathematics, II, vol. 22, AMS, Providence, RI, 1985, pp. 327–336.
[16] R.B. Lehoucq, D.C. Sorensen, C. Yang, ARPACK User's Guide, SIAM Publication, 1998.
[17] M. Hammache, M. Gharib, An experimental study of the parallel and oblique vortex shedding from circular cylinders, J. Fluid Mech. 232 (1991) 567–590.
[18] D. Barkley, R.D. Henderson, Three-dimensional Floquet stability analysis of the wake of a circular cylinder, J. Fluid Mech. 322 (1996) 215–241.
[19] C.H.K. Williamson, Vortex dynamics in the wake of a cylinder, in: S.I. Green (Ed.), Fluid Vortices, Kluwer, Dordrecht, 1995, pp. 155–234.
[20] M. Strelets, Detached-eddy simulation of massively separated flows, AIAA Paper No. 2001-0879, 2001.
[21] F.S. Sherman, A low-density wind tunnel study of shock wave structure and relaxation phenomena in gases, NACA Tech. Note 3298, 1955.